International Journal of Concrete Structures and Materials

Open Access

Enhanced Predictive Modelling of Steel Corrosion in Concrete in Submerged Zone Based on a Dynamic Activation Approach

Zahid Mohammad Mir[1*], Daniel Höche[1,2], Celestino Gomes[3], Rui Sampaio[3], Alexandre C. Bastos[3], Philippe Maincon[4], M. G. S. Ferreira[3] and Mikhail L. Zheludkevich[1,5]

Abstract

A numerical model for enhanced service life prediction of concrete infrastructure is presented which includes transient analysis of processes during corrosion initiation as well as propagation stage. The temporal and spatial transition of Steel–Concrete Interface during depassivation events is described by a randomly varying chloride threshold function. As such random activation events can be accounted for, rather than having to pre-describe the anode size and location as in many existing models. The aim of the study is to investigate random spatial activation events in concrete structures in submerged zones based on dynamically changing boundary conditions on the rebar surface to control transition from passive to active state. Investigations are carried out to realize the sustainability of corrosion processes in limiting oxygen concentrations in dissolved seawater. The model showcases the numerical architecture, the associated concept of randomly varying chloride threshold and predicts that among other factors, the rate of oxygen strongly influences corrosion rate in submerged locations.

Keywords: rebar corrosion, chloride-induced depassivation, finite element method, submerged zone

1 Introduction

The corrosion-induced degradation of reinforced concrete (RC) structures is a well-known issue in the infrastructure community and is still one of the biggest challenging problems affecting structures worldwide (Page 1975; Tuutti 1982; British Cement Association 1997; Bertolini et al. 2013) amounting to losses in billions (Koch et al. 2001). The current societal, economic and technological challenges due to corrosion of steel in concrete outweigh the ongoing efforts and, as such, more scientific investment is necessary in this direction (Angst 2018). Furthermore, the situation is foreseen to get even worse due to the gradual aging of the infrastructure especially in developed countries and, to

some extent, in developing countries as well (Angst and Elsener 2017). Although, the corrosion-induced degradation can be caused by a variety of factors such as carbonation, chloride, acid exposure etc., the present work focusses entirely on chloride-induced corrosion of steel in concrete. The porous nature of the concrete allows the chloride ions to pass through it, ultimately reaching the rebar surface via a shortest path, i.e. concrete cover. The attainment of sufficiently high chloride concrete at the rebar surface marks the beginning of the corrosion process. This duration of time is called the initiation phase and can last several years or even decades, depending on the quality of concrete and exposure conditions. The corresponding chloride concentration is called critical chloride threshold (Cl_{th}) level.

In principle, the numerical calculation of corrosion parameters inside concrete depends on the accurate modelling of transport processes inside concrete for water content, temperature, chloride and oxygen, coupled with electrochemical processes at the Steel–Concrete Interface (SCI). Furthermore, one has to account

*Correspondence: zahid.mir@hzg.de
[1] Institute of Materials Research, Helmholtz-Zentrum Geesthacht Centre for Materials and Coastal Research, Max-Planck Str. 1, 21502 Geesthacht, Schleswig-Holstein, Germany
Full list of author information is available at the end of the article

Mir *et al. Int J Concr Struct Mater*   (2019) 13:11

Page 2 of 18

the mechanical effects of the generated rust products, such as creep around the rebar and eventually account for the induced damage in concrete (Ozbolt et al. 2012). Currently, there is a large number of numerical models (Bazant 1979; Page et al. 1981; Balabanic et al. 1996; Zhang and Gjorv 1996; Andrade et al. 1997; Thomas and Bamforth 1999; Glass and Buenfeld 2000; Ishida et al. 2009; Marsavina et al. 2009; Ozbolt et al. 2010, 2011, 2014) which are able to accurately model the above mentioned processes, i.e. before and after depassivation. However, very few of these focus on the accurate description of activation events and spatial location of active zones. In most of these models, either the anode size is pre-described or the initiation stage is decoupled from the propagation stage. This is contrary to what is observed in real life structures, where there is a random generation of activation events i.e. at SCI. The activation events demonstrate a stochastic temporal and spatial generation due to the heterogeneity at the SCI. This heterogeneous nature of the SCI has been confirmed in many studies (Angst and Elsener 2015; Angst et al. 2017). Given this random nature of SCI, an approach is proposed based on a varying chloride threshold ($f^p_{Cl\_T}$) to account for the random and probabilistic nature of SCI with regard to varying Cl_{th} levels. Therefore, in this study, a varying chloride function $f^p_{Cl\_T}$ accounts for factors which arise due to inhomogeneity at SCI. Examples of local factors are Pre-cracks (Borosnyói and Balázs 2005), air voids (Angst et al. 2017), interfacial transition zone (ITZ) and associated chemistry (Page 1975; Gjorv 1995; Horne et al. 2007; Jakobsen et al. 2016; Vollpracht et al. 2016), presence of mill scale (Ghods et al. 2011; Karadakis et al. 2016), pre-existing rust (Angst and Elsener 2015; Stefanoni et al. 2015), passive film (Hansson et al. 2006; Poursaee and Hansson 2007; Ghods et al. 2009; Zhang and Poursaee 2015; Poursaee 2016), bleed zones (Mohammed et al. 2002; Castel et al. 2003; Soylev and Francois 2003; Castel et al. 2006; Horne et al. 2007), nature of steel (Ray et al. 1997; Nikolaou and Papadimitriou 2004; Scully and Hurley 2007; Cadoni et al. 2013), structural loads (Feng et al. 2011a, b) as shown in Fig. 1 and as well as the bar-orientation (Angst and Elsener 2015) etc. The combination of these varying parameters leads to varying temporal and spatially Cl_{th} levels and consequently varying time for corrosion initiation.

Varying chloride threshold levels were experimentally measured by Silva et al. (2013) and the results indicated that along the SCI a range of chloride levels could be observed. Threshold levels varied between 0.15 and 1.5 wt% of concrete. Similar results have been extensively documented by Angst et al. (2009).
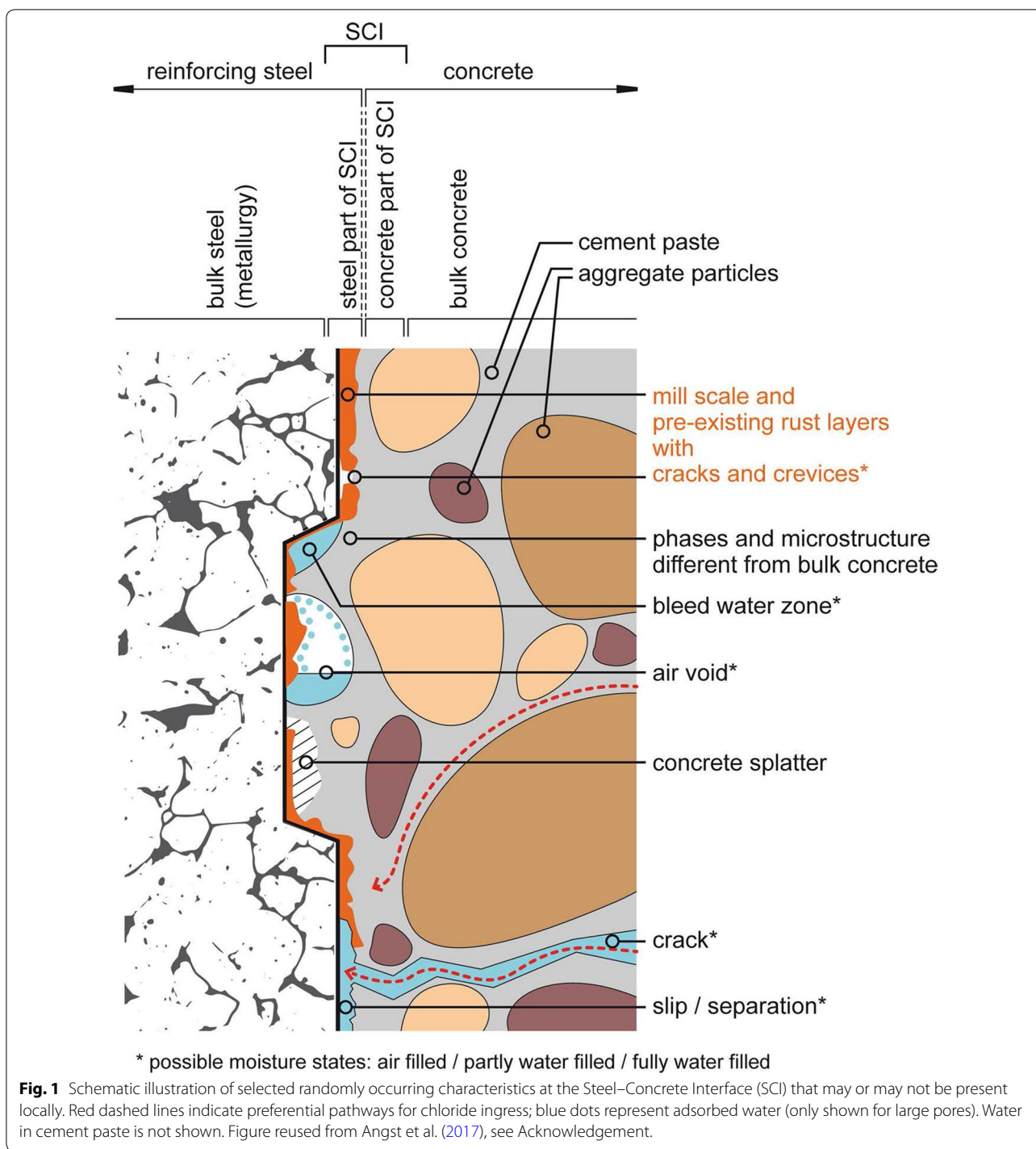
These uncertainties at SCI can be weighed against a central factor of a variable threshold or a local threshold. As a result a probabilistic function is required to account for the spatial variation of Cl_{th} along the rebar surface. As such, anode location and size are not pre-described in this model and anodic activation can occur wherever the local Cl_{th} has been exceeded (Michel 2013) as described by $f^p_{Cl\_T}$. Furthermore, initiation and propagation phases are combined together in a single numerical model.

Recent experimental findings from a 20 year exposure history (Boubitsas et al. 2014) of structures exposed to marine environment in the Träslövsläge field site on the west coast of Sweden have revealed that chloride attack is far more severe in the submerged zone than in the splash zone. Therefore, more attention is required to explore the corrosion characteristics of infrastructure in the submerged zones. Similar data was recorded by extensive field studies of concrete samples submerged in seawater in different geographical locations (Lindvall 2003). Another motivation is that, historically, submerged zones have received little attention, which could be mostly attributed to difficulties in conducting experimental work. Few case studies are reported in the literature. Recent field assessment of decommissioned bridge piers in submerged zone in south Florida listed by Walsh (2015) has revealed severe localized corrosion in the submerged zones with localized active regions up to 20 cm in length. Therefore, submerged zone has been chosen as the exposure scenario for the numerical model.

In addition, numerical treatment of rust generation has been included in the model by employing solubility criteria (Yan et al. 1993; Deslouis et al. 2000; Hoche 2015). This includes modelling of surface reactions leading to rust layer growth occurring due to precipitation of corrosion products such as $Fe(OH)_2$. The presented model represents a continuum of a coupled system of field equations with accompanying non-linear boundary conditions. The finite element method has been employed (Belytschko et al. 2000, 2014) to solve the resulting system of equations. Several fundamental assumptions have been considered, balancing accuracy versus computational cost. The assumptions include:

a. Adsorption and desorption hysteresis for moisture are not considered (Ozbolt et al. 2016).
b. Formation of rust layer is attributed to generation of $Fe(OH)_2$ as a primary rust product. However, many other products have been identified (Vera et al. 2009).
c. Mechanical damage, due to rust generation is excluded from the model. This is left for future studies.
d. Theory of dilute solutions is employed.

Mir *et al. Int J Concr Struct Mater*   (2019) 13:11

Page 3 of 18

Fig. 1 Schematic illustration of selected randomly occurring characteristics at the Steel–Concrete Interface (SCI) that may or may not be present locally. Red dashed lines indicate preferential pathways for chloride ingress; blue dots represent adsorbed water (only shown for large pores). Water in cement paste is not shown. Figure reused from Angst et al. (2017), see Acknowledgement.

e. Uniform rebar surface conditions are considered. Variation of SCI parameters are included inside $f^p_{Cl\_T.}$

f. Potential-dependent variation of chloride threshold is not included, the reader is directed to works of Sagüés et al. (2014), Walsh (2015).

g. Chemical activity effects are not considered.

In the present paper, a 2D numerical model is presented wherein transport processes leading to corrosion initiation are coupled with electrochemical processes. Non-linear boundary conditions are used at the rebar surface to account for corrosion currents. A representation of concrete pore solution is used as electrolyte medium.
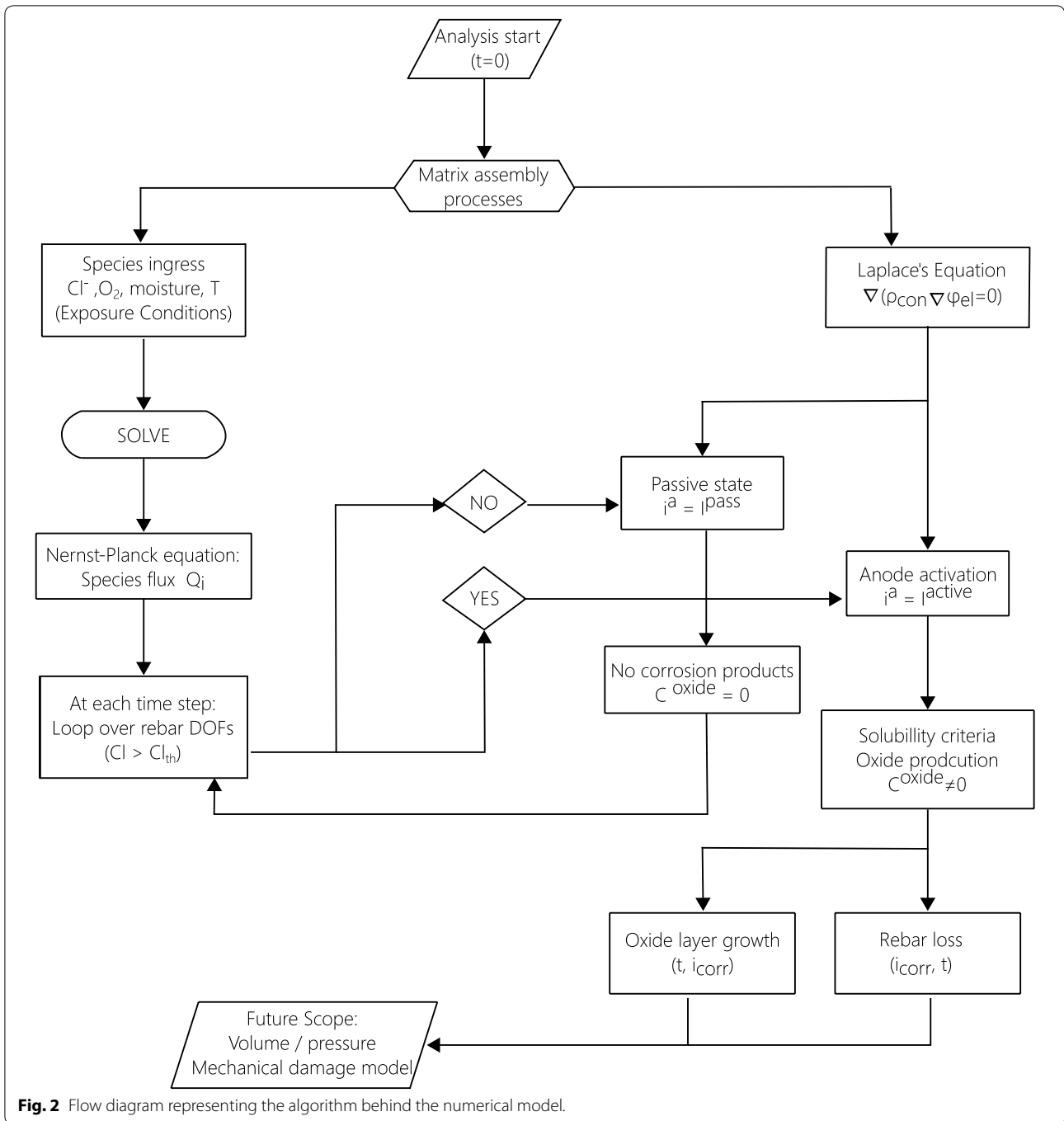
Mir *et al. Int J Concr Struct Mater*   (2019) 13:11

Page 4 of 18

Processes leading to hydration of concrete are ignored: sufficiently aged concrete with hydration age ($T_{hy} > 180$ days) is considered. A simplified 2D geometry is employed to exhibit the FEM based coupled model in order to investigate the transport and corrosion processes. The coupling of non-mechanical processes with mechanical damage processes is under development.

2 Mathematical Formulation of Physical Processes

This study is focused on modelling transport and corrosion processes applicable to submerged zones. Governing field equations and related boundary conditions are presented. It is assumed that the concrete is in a mature condition ($T_{hy} > 180$ days): hydration processes are mostly completed and as such chloride diffusion can be assumed to be independent of the degree of hydration (Tang and Nilsson 1996). The electrolyte is defined using a concrete pore solution from Johannesson et al. (2007) and has been adopted for initial electrolyte concentration, see Table 1. All processes leading to corrosion-initiation, such as moisture transport, oxygen transport, chloride transport and other governing physical phenomena are described. The general structure of the computational model is shown in Fig. 2.

2.1 Multi Ion Laplace–Nernst Planck Model

Concrete is an intrinsically porous quasi brittle material. The theory of dilute solutions in porous media has been adopted for modelling transport of ions in water filled pore space inside bulk concrete. The movement of ions inside the pore solution is carried out using a set of extended Nernst–Planck equations for each ion. The model tries to accommodate as many ions as possible to mimic the realistic cementitious environment as it has been pointed out by Karadakis et al. (2016) that the diffusion rate of each ion inside the pore solution is governed by the electrolyte potential of the entire ionic solution as well as the concentration gradient. The flux of each specie Q_i (mol/m²/s) through the electrolyte pore system can be written as

$$Q_i = -\left(D_i \nabla C_i + z_i U_{i_{mob}} F C_i \nabla \emptyset_{el}\right) + C_i \boldsymbol{u} \tag{1}$$

and the mass balance for each specie is written as

$$\varphi_p \frac{\partial C_i}{\partial t} = -\nabla \cdot \left(\varphi_p Q_i\right) + m_{r\_i} \tag{2}$$

where φ_p denotes the capillary porosity of mature concrete (m³ of voids per m³ of concrete), C_i denotes the concentration of each pore ion specie, $D_i = D_i^w \tau t_t$ is the effective diffusion coefficient of each specie, as one has to account for the effects of pore system structure (Johannesson et al. 2007; Ishida et al. 2009) such as tortuosity t_t and τ is a model parameter for each specie with charge number z_i. The ionic mobility coefficient is computed from Einstein's relation: $U_{i_{mob}} = \frac{D_i}{(R_{gas}T)}$ with, R_{gas} as the gas constant and T as the ambient temperature in K. $\emptyset_{el}$ is the electric potential, F is Faradays constant, m_{r_i} is the source/sink term to account for dynamic ion–ion and ion–oxide interactions and $\boldsymbol{u}$ is the convection term in the electrolyte flow velocity vector, having a major effect (Hoche 2015) on corrosion under flow. Here $\boldsymbol{u}$ is set to zero as mass transfer under flow does not exist inside concrete thereby, excluding the effects of convection. The approach includes the ionic species as shown in see Table 1.

For precipitates and deposition of solid species especially corrosion products, the diffusion term is set to zero in the Nernst–Planck equation. Furthermore, the model assumes electro-neutrality at each point in the electrolyte domain by assuming charge conservation at each time step in the analysis according to the relation:

$$\sum_{bulk} z_i C_i = 0 \tag{3}$$

The resulting electric current density $\boldsymbol{i}_{el}$ in the electrolyte due to transport of charge carrying ions through it, is described by Faraday's Law:

$$\boldsymbol{i}_{el} = F \sum_{bulk} z_i Q_i \tag{4}$$

Apart from charge and mass conservation, electrical neutrality is maintained and can be written as:

$$\nabla \cdot \boldsymbol{i}_{el} = 0 \tag{5}$$

The above expression can be rewritten to include the concrete resistivity ρ_{el} which is directly dependent on

Table 1 Pore solution and pore system characteristics (Johannesson et al. 2007).

Species	Cl⁻	Na⁺	OH⁻	Ca²⁺	K⁺	SO₄²⁻
$D_i^w \times 10^{-9}$ (m²/s)	2.2	1.33	5.28	0.79	1.96	1.07
C_i (t = 0) (mol/m³)	0	85	300	10	213	9
Scaling parameter τ	0.1	0.4	1	0.2	0.4	1
Tortuosity t_t	0.015	0.015	0.015	0.015	0.015	0.015

Mir *et al. Int J Concr Struct Mater*   (2019) 13:11

Page 5 of 18

Fig. 2 Flow diagram representing the algorithm behind the numerical model.

the degree of saturation S^w of concrete as well as the capillary porosity φ_p.

$$\nabla \cdot \left(1/\rho_{el} \left(S^w, \varphi_p \right) . \nabla \emptyset_{el} \right) = 0 \tag{6}$$

For a constant resistivity, Eq. (6) reduces to a standard Laplace equation for the domain.

$$\nabla^2 \emptyset_{el} = 0 \tag{7}$$

The above equation is solved for the distribution of electric potential as the field variable in order to model the movement of ions against an electrical field and to use electrochemical boundary conditions at SCI which will be discussed in the forthcoming sections. The conductivity and oxygen diffusivity in concrete in the submerged zone has been interpolated from Fig. 3.

Mir *et al. Int J Concr Struct Mater*   (2019) 13:11

Page 6 of 18
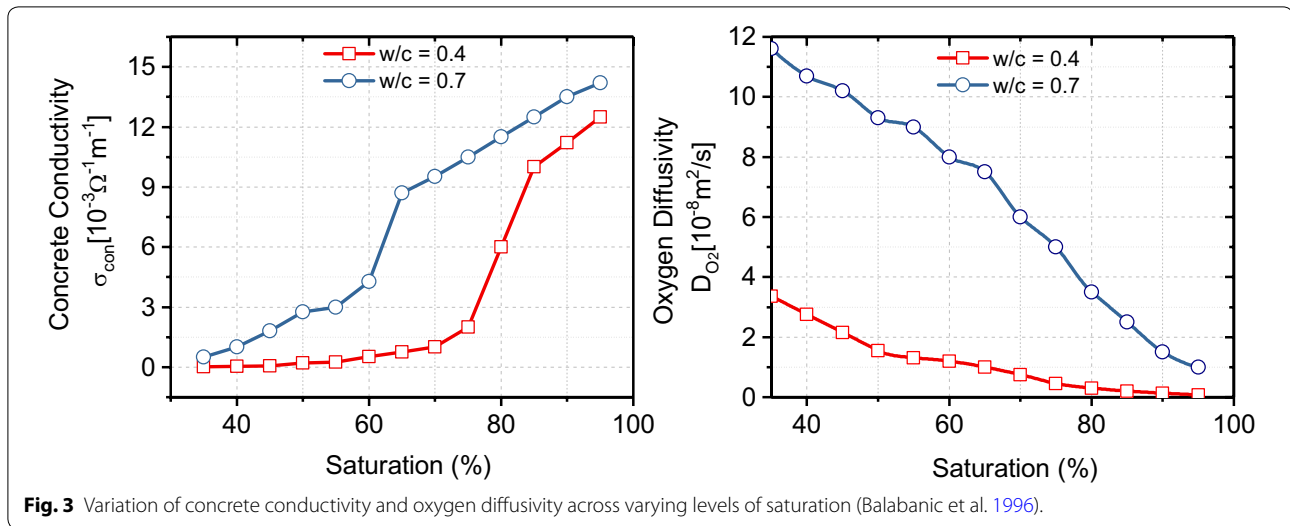
Fig. 3 Variation of concrete conductivity and oxygen diffusivity across varying levels of saturation (Balabanic et al. 1996).

2.2 Capillary Water Transport

Moisture transport is included in the model by considering diffusion-based movement of moisture through the capillary network under an external gradient. Richards's equation is used to model moisture movement as a volume fraction of bulk concrete (Tang and Nilsson 1996; Ozbolt et al. 2010).

$$\frac{\partial \theta_h}{\partial t} = \nabla \cdot [D_h(\theta_h)\nabla \theta_h] \tag{8}$$

where, $\theta_h = S^w \varphi_p$ is the volume fraction of pore water inside concrete and $D_h(\theta_h)$ is the diffusivity coefficient of capillary water inside concrete. Previous studies (Leech et al. 2003; Ozbolt et al. 2010) have denoted capillary water as a nonlinear function of initial and saturated water contents. This nonlinear expression is denoted as

$$D_h(\theta_h) = D_{0\_h}e^{n\bar{\theta}_h} \tag{9}$$

with,

$$\bar{\theta}_h = (\theta_h - \theta_{0\_h})/(\theta_{t\_h} - \theta_{0\_h}) \tag{10}$$

where, D_{0_h}, n, $\bar{\theta}_h$, θ_{0_h}, θ_{t_h} are the initial diffusivity coefficient, shape term, reduced water content, initial and saturated water content respectively, see Table 2. In this work, for submerged conditions, $S^w = 1$ has been considered.

2.3 Chloride Binding

It is widely accepted that the chloride binding capacity of the bulk cement is greatly responsible for extending the corrosion initiation stage. Various cement phases

Table 2 Parameters included in the computational model.

Parameter	Symbol	Value	Unit
Limiting capillary water permeability	D_{0_h}	2.2×10^{-10}	m²/s
Shape factor	n	6.4	–
Initial fraction of water content	θ_{0_h}	0.01	m³/m³
Saturated water content	θ_{t_h}	0.1	m³/m³
Concrete porosity	φ_p	0.1	m³/m³
Hydration age	T_{hy}	> 180	Days
Binding rate coefficient for chloride ions	α_{rc}	1×10^{-5}	1/s
Isotherm calibration factor	β	0.7	–
Deposition constant Fe(OH)₂	$K_{Fe(OH)_2}^{int}$	3.7×10^{-1}	1/s
Solubility product of Fe(OH)₂	$K_{Fe(OH)_2}^{sp}$	8×10^{-6}	mol³/m⁹
Binder content	W_{binder}	350	kg/m³
Density of concrete	ρ_{con}	2400	kg/m³
Gas constant	R_{gas}	8.31×10^{-3}	kJ/mol/K
Thermal conductivity of concrete	λ	2.1	W/m/K
Specific heat capacity of concrete	c	900	J/kg/K
Molar mass of Cl⁻	M_{Cl}	0.035	kg/mol

exhibit varying chloride binding capabilities. X-ray photoelectron spectroscopy (XPS) investigation of Johannesson et al. (2007) demonstrated that AFm phases possess significantly higher binding capabilities compared to CSH phases, whereas experiments by Hirao et al. (2005) concluded otherwise. However, CSH due to its highest volume fraction certainly contributes the most to chloride binding. Total binding of chloride is a combination of physical binding of chloride with pore walls as well as chemical binding forming Friedel's salt ($3CaOAl_2O_3 \cdot CaCl_2 \cdot 10H_2O$) at lower concentrations and Küzel's salt ($3CaO \cdot Al_2O_3 \cdot 0.5CaSO_4 \cdot 0.5CaCl_2 \cdot 11H_2O$) at

Mir et al. Int J Concr Struct Mater   (2019) 13:11

Page 7 of 18

higher concentrations (Zibara 2001). In this work, the overall binding has been expressed with a chloride isotherm depicting a linear relationship between free chloride in the pore solution and the bound chloride.

$$\varphi_p \frac{\partial C_{Cl}}{\partial t} = -\nabla.(\varphi_p Q_{Cl}) + m_{r\_Cl} \qquad (11)$$

$$\frac{\partial C_{clb}}{\partial t} = \alpha_{rc}(\beta C_{cl} - C_{clb}) = -m_{r\_Cl}$$

C_{Cl} is free chloride concentration of pore solution in (mol/m^3), and C_{clb} is bound chloride expressed in (kg/m^3) of concrete. α_{rc} is a binding rate constant and β is a model parameter (Saetta et al. 1993).

2.4 Oxygen Transport
The transport of oxygen from the external environment to the SCI is modelled entirely based on diffusion and as such the mass balance for oxygen can be written as

$$\varphi_p \frac{\partial C_{O_2}}{\partial t} = \nabla \cdot \left(\varphi_p D_{O_2}(S^w, \varphi_p)\nabla C_{O_2}\right) \qquad (12)$$

The diffusion of oxygen is high in unsaturated concrete and considerably lower in water saturated concrete. The diffusion coefficient of oxygen has been taken from data extrapolation of Balabanic et al. (1996), see Fig. 3.

2.5 Depassivation Based on Random Distribution of Chloride Threshold
In many previous modelling approaches (Balabanic et al. 1996; Kim and Kim 2008; Michel 2013), a pre-defined anode size and location is used for numerical analysis, which is quite contrary to what is observed in the electrochemical testing of concrete. Activation events are particularly random in un-cracked members. For members experiencing pre-cracking or flexural cracking, activation events can occur directly at the crack location on the SCI (Ozbolt et al. 2010) and can be preassigned. Furthermore, in many models a single chloride threshold value is used, whereas for similar concrete mix and laboratory conditions, a clear variability is observed in depassivation as reported in the recent experiments of Angst and Elsener (2017).

Apart from the chloride concentration at the rebar, there are other randomly varying factors which play a crucial role in depassivation. As mentioned previously, these factors include pre-cracks, air voids, water channels, bar orientation, rebar surface conditions and workmanship (Angst et al. 2017). As an example, the

presence of small air voids at the SCI can have a strong shielding effect and retard the depassivation of rebar at those locations, because a high pressure is required to fill these air voids and might take decades to completely fill in. On the contrary, water pockets usually found under horizontally placed rebars can lead to a faster attainment of depassivation. In continuum-based models, these variable factors at the SCI cannot be easily accounted for, due to their probabilistic nature and difficulties in experimental quantification. Several models would be required to investigate the effect of each factor, thereby considerably increasing the computational effort. Therefore, in this study, we have included these varying parameters into a randomly distributed mathematical function $f^p_{Cl\_T}$ with varying chloride threshold limits along the rebar surface. The range of Cl_{th} is obtained from experiments by Alonso et al. (2000) with $0.39 < Cl_{th} < 1.16$ (free Cl^- as a percentage of binder weight) and is used as end limits for $f^p_{Cl\_T}$. This function includes numbers varying within the Cl_{th} range at equal intervals and fitted with a smooth cubic spline function. Anodic activation is therefore accounted in the model with spatial and temporal resolution at locations where the chloride content has exceeded its randomly assigned value at a particular location on the rebar surface. The numerical model is able to change the metal dissolution currents at these spatial locations. Other models employing a varying chloride threshold include works of Sagüés et al. (2014), Walsh (2015) and Michel (2013).

2.6 Electrochemical Boundary Conditions
The electrochemical reactions occurring at the rebar interface follow Faraday's law and can be described as oxidation of iron ($2Fe \rightarrow 2Fe^{2+} + 4e^-$) and consumption of oxygen at the cathodic sites, leading to production of hydroxyl ions ($O_2 + 4H_2O + 4e^- \rightarrow 4OH^-$). At the very beginning of the service life of RC structures, the rebars are in a passive state. Once the chloride threshold is exceeded at a particular point on the rebar surface, anodic activation is enabled at this particular location leading to metal loss and oxide generation. The model is able to dynamically make this transition by constantly looping over all mesh elements at rebar surface in each time step to check for the exceeded local Cl_{th} levels. Due to a limited number of elements on the rebar surface as compared to the bulk, this step is deemed not to be computationally expensive. The electrochemical state of rebar in passive and active stage is shown schematically in Fig. 4.

Tafel like extrapolation of the Butler–Volmer relations have been used for electrode kinetics at the interface. It

Mir *et al. Int J Concr Struct Mater*   (2019) 13:11

Page 8 of 18

Fig. 4 Schematic representation of the electrochemical kinetics of steel in concrete undergoing depassivation. **a** Passivated condition ($Cl < Cl_{th}$). **b** Depassivated-condition ($Cl > Cl_{th}$).
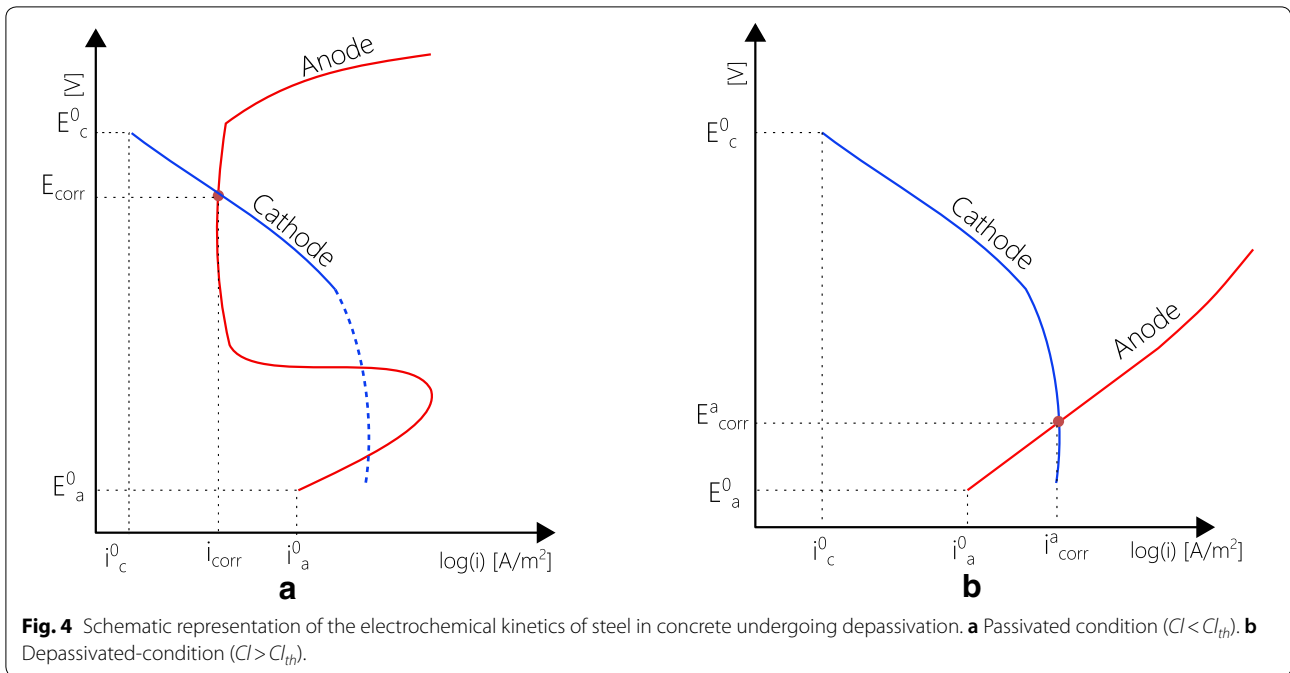
is assumed that anodic parts are subjected to activation polarization as:

$$i_a = \begin{cases} i_a^{pass}, & Cl < Cl_{th}(x) \\ i_a^0 \cdot e^{2.3\left(\emptyset_{el} - \emptyset_a^0\right)/\beta_a}, & Cl \geq Cl_{th}(x) \end{cases} \quad (13)$$

where, i_a is the anodic current density (A/m^2) and $i_a^{pass} = 10^{-4}$ A/m^2 is the passive current density as reported (Hansson 1984; Poursaee and Hansson 2007). The change from passive to active current is done using a smoothed Heaviside function to avoid computational instabilities. Here i_a^0 is the exchange current density (A/m^2), $\emptyset_{el}$ is the electric potential (V) as calculated from Laplace equations (Eq. 7) on the interface, $\emptyset_a^0$ is the equilibrium potential and β_a is the anodic Tafel slope in (V/dec).

For the cathodic half-cell reaction, the transport of oxygen through the concrete cover and its consumption at the cathodic sites leads to a limiting oxygen diffusion current density for the attainment of a continuous flux of oxygen. The cathodic reaction is under activation and concentration polarization and is expressed based on works of Kranc and Sagues (1994) thereby including the concentration of oxygen at the SCI as:

$$i_c = -i_c^0 \cdot \left(\frac{C_{O_2}^{SCI}}{C_{O_2}^{ext}}\right) e^{2.3\left(\emptyset_{el} - \emptyset_c^0\right)/\beta_c} \quad (14)$$

where, i_c is the cathodic current density (A/m^2), i_c^0 is the exchange current density (A/m^2), $\emptyset_c^0$ is the equilibrium potential for the cathodic and β_c is the cathodic Tafel slope in (V/dec). $C_{O_2}^{SCI}$ is the concentration of oxygen at the SCI, $C_{O_2}^{ext}$ is the external concentration of the oxygen at the concrete cover.

At the rebar interface, O$_2$ is consumed whereas OH$^-$ ions are produced as a consequence of reduction reaction. Similarly, Fe^{2+} ions are produced due to oxidation of metal at the interface. For the cathodic sites, according to Faradays law, the number of oxygen molecules reduced per unit surface area per unit time at the SCI is given by the relation:

$$i_c = zFQ_{O_2}\big|_{SCI} \quad (15)$$

where, Q_{O_2} is the flux of oxygen in (mol/m^2/s) molecules reduced at the interface and z = 4 is the number of electrons transferred in the cathodic half-cell reaction. One the other hand, the oxygen influx due to diffusion can be expressed as:

$$Q_{O_2} = -n \cdot \left(D_{O_2}\nabla C_{O_2}\right)\big|_{SCI} \quad (16)$$

The balance between the O$_2$ molecules reduced at the rebar and the O$_2$ molecules arriving to the rebar surface with normal n from the nearby surrounding concrete. The conservation of oxygen then leads to:

$$\frac{i_c}{zF} = -n \cdot \left(D_{O_2}\nabla C_{O_2}\right)\big|_{SCI} \quad (17)$$

Mir et al. Int J Concr Struct Mater   (2019) 13:11

Page 9 of 18

Similarly the production of hydroxyl ions at the interface can be expressed as:

$$i_c = zFQ_{OH^-}|_{SCI} \tag{18}$$

where, Q_{OH^-} is the production flux in of OH^- ions and $z = 4$. For the anodic half-cell reaction, the production of ferrous ions can be accounted from the anodic current density as:

$$i_a = zFQ_{Fe^{2+}}|_{SCI} \tag{19}$$

where $Q_{Fe^{2+}}$ is the flux of ferrous Fe^{2+} ions and $z = 2$ is the number of electrons transferred in the anodic half-cell reaction. A schematic representation of ionic transport is depicted in Fig. 5a.

2.7 Heat Transport

The transport of heat within the bulk concrete leads to the distribution of temperature and can be expressed (Ozbolt et al. 2010) as:
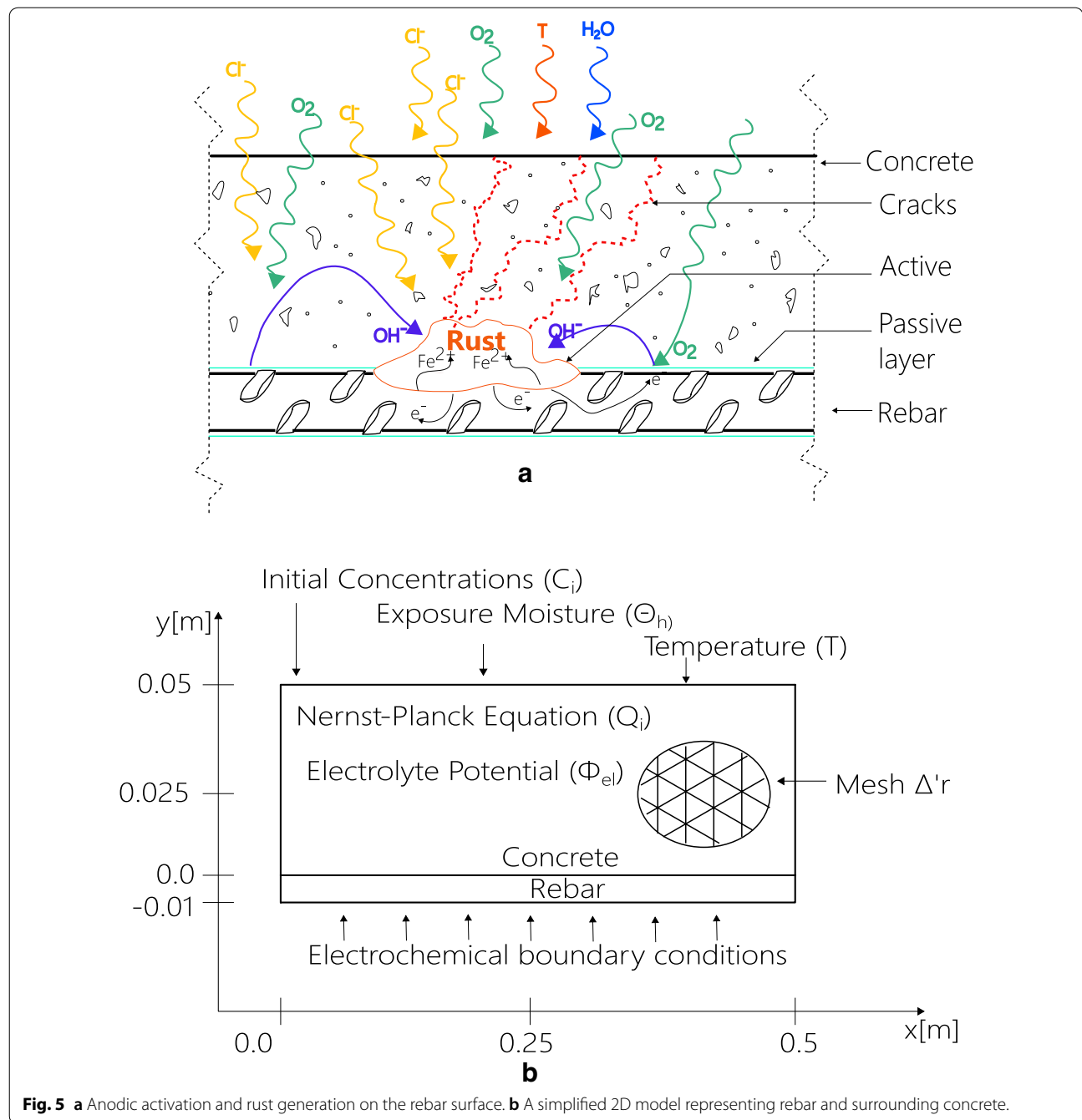
Fig. 5 **a** Anodic activation and rust generation on the rebar surface. **b** A simplified 2D model representing rebar and surrounding concrete.

$$\lambda(\Delta T) - c\rho_{con}\frac{\partial T}{\partial t} = 0 \tag{20}$$

where, T is the field variable for temperature distribution, λ is the thermal conductivity of concrete in (W/m/K), c is the thermal heat capacity of concrete (kg/m^3) and ρ_{con} is the density of concrete (kg/m^3).

2.8 Solubility Criteria for Self-Induced Oxide Production

Different experimental investigations have revealed a number of corrosion products formed during corrosion of steel inside concrete (Yamashita et al. 2005; Oluwadare and Agbaje 2007). Although the surface of hot rolled carbon steel is already covered with stable protective mill scale oxides, these oxides can end up dissolving once the chloride threshold is attained revealing the bare metal. As a continuation of electrochemical reactions, corrosion products are formed at the SCI and immediately start filling the concrete pores around them, forming a corrosion accommodating region (CAR). However, these corrosion products have a higher volume than that of the parent metal, leading to a build-up of pressure at SCI. This pressure increases with time, leading to formation of micro cracking zones around the SCI and in due course of time, eventually forming cracks, extending radially outwards and also longitudinally along the rebar length. The type of corrosion product depends on the exposure scenario. However, it is widely accepted that $Fe(OH)_2$ is the first corrosion product (Vera et al. 2009) formed immediately after depassivation. In the present model only $Fe(OH)_2$ has been considered for model simplicity according to the following reaction:

$$Fe^{2+} + 2OH^- \rightarrow Fe(OH)_2 \tag{21}$$
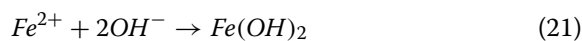
The above reaction describes the formation of $Fe(OH)_2$ in the pore solution. The corresponding reaction rate can be expressed using an interface deposition constant calculated using the solubility product as:

$$\frac{\partial C_{Fe(OH)_2}}{\partial t} = m_{r\_int}^{Fe^{2+}} = K_{Fe(OH)_2}^{int}$$
$$\times (C_{Fe^{2+}}C_{OH^-}^2 - K_{Fe(OH)_2}^{sp}) \times f^{Ksp} \tag{22}$$

where, $f^{ksp} = \begin{cases} 1 & \left([Fe^{2+}][OH^-]^2 - K^{sp} > 0\right) \\ 0 & \left([Fe^{2+}][OH^-]^2 - K^{sp} < 0\right) \end{cases}$

is a step function which triggers oxide production only when the concentration of the constituent ions exceed the solubility product of the corresponding oxide. Oxide production occurs only at those points where $K_{Fe(OH)_2}^{sp}$

is exceeded. The formation rate of the oxide and the interface rate constant $K_{Fe(OH)_2}^{int}$ are based on works of Höche (2015) and Yan et al. (1993). These model constants signify a two dimensional mathematical description of the oxide film, representing hydroxide formation and its adhesion to the rebar surface. The solubility constant $K_{Fe(OH)_2}^{sp}$ is chosen to capture the initiation point of precipitation.

3 Numerical Case Study

A simplified 2D geometry has been chosen as shown in Fig. 5b to solve the above-mentioned coupled system of non-linear equations and boundary conditions. All the processes prior to cracking of concrete are described. The concrete and steel domains are discretized using finite element method. The weak forms were derived using the method of Galerkin's weighted residual (Zienkiewicz 1972; Belytschko et al. 2014) and solved via an implicit time integration scheme using COMSOL Multiphysics software. The detailed expression of the weak forms for the mentioned partial differential equations are not presented in the paper for the sake of brevity.

The domains Eqs. (2) and (7), represent a system of highly nonlinear equations which are decoupled, linearized and the resulting equation residuals are solved using a damped Newton's Raphson iterative method with a constant predictive slope (Bischoff et al. 2014). A regular mesh was constructed using Lagrange-based triangular elements. Mesh convergence studies were carried out to find an element size with balancing computational efficiency and numerical accuracy.

The average physical computational time was around 12 h, using a 44 core, 128 GB RAM workstation. An adaptive time stepping scheme was used with a minimum time step of 0.0864 h and a maximum time step of 48 h. Smaller time steps are employed during change of electrochemical boundary conditions to have better convergence. The simulated duration was 41 years.

The future development of the current model is in progress wherein the numerical coupling of the above mentioned non-mechanical system of equations with a damage based mechanical material model for concrete is in progress. The generation of cracks due to the expansion of corrosion products will be also simulated for 3D structural members in submerged conditions.

3.1 Exposure Conditions

Submerged sea water exposure has been chosen as the exposure conditions. The corresponding external chloride concentration $C_{Cl^-}^{ext}$ is taken equal to 450 mol/m^3 (16 g/l) and the initial pore solution chloride concentration is shown in Table 1. The initial oxygen concentration is $C_{O_2} = 0.15$ mol/m^3. The concentration of

external dissolved seawater oxygen concentration is set to $C_{O_2}^{ext} = 0.28$ mol/m³. Electric insulation is maintained by enforcing $\vec{n} \cdot i_{el} = 0$ on the external model boundaries, where $\vec{n}$ is the normal vector to mesh boundary. The condition $\vec{n} \cdot Q_i = 0$ maintains symmetric boundary conditions, where the subscript i denotes all mobile chemical species inside the bulk.

4 Results and Discussion

The central goal of this study is to present the effect of a variable threshold and the associated numerical architecture to handle the change of boundary conditions from passive state to active state in time. The paper focusses on the numerical architecture and the underlying concept. The validation of this model is performed using observation of Perez and Chlorides (1999), Ozbolt et al. (2011), Michel (2013) who studied the corrosion of steel in concrete under various degrees of saturation. The exposure case studied here is the submerged zone.

4.1 Effect of a Variable Threshold Function

Randomly varying chloride function $f^p_{Cl\_T}$ as discussed previously is applied on the exposed rebar surface. $f^p_{Cl\_T}$ controls the activation at all spatial locations on the rebar as shown in the Fig. 6a, b. Prior to activation, the entire rebar surface undergoes uniform passive corrosion with a passive corrosion current density of $1 * 10^{-4}$ A/m² as reported by experiments performed by Poursaee and Hansson (2007) and computational studies performed by Sagüés et al. (2014).

The passive stage results in a negligible rebar loss and the structural member is said to be in its initiation stage. The activation on the rebar surface depend on the accumulation of free chlorides at that location. The local chloride threshold is calculated as a function of binder weight using Eq. (23).

$$Cl_{th} = \left(\frac{C_{Cl}^{free} M_{Cl} \varphi_p \cdot 100}{W_{binder}} \right) \quad (23)$$

where, Cl_{th} is the chloride threshold as a weight percent of binder weight W_{binder}, which in turn is expressed in (kg binder per m³ of concrete), C_{Cl}^{free} is the free concentration of chloride at the rebar surface in (mol/m³) of pore solution, M_{Cl} is the molar mass of chloride in (kg/mol), φ_p is the capillary porosity in (m³ pores per m³ of concrete).

The chloride transport is modelled by using Nernst–Planck equation (Eq. 11). As the local chloride threshold as defined by $f^p_{Cl\_T}$ at a particular location on the rebar is exceeded, the boundary conditions on that point change from passive to active, thereby following Butler–Volmer Kinetics (Eqs. 13, 14). The effect of the variable chloride

threshold and changing of boundary conditions on the rebar can be better visualized in terms of electrochemical parameters (Fig. 4).

Degradation is monitored at two locations referred as location 1 and location 2 (Fig. 6a). At location 1 (Fig. 6b), the critical chloride threshold $f^p_{Cl\_T}$ is equal to 0.39 (%W_{binder}) and is exceeded in 14.35 years. The pre-peak curve in Fig. 6c1 represents the initiation stage. The post-peak curve designates the stage of active corrosion. The attainment of critical chloride threshold results in switching boundary conditions to activated Butler–Volmer kinetics with a peak current density of 0.0285 A/m². This stage marks the end of the initiation period and the structure is said to be in degradation stage, although other regions of the rebar still maintain a passive layer. The corrosion current density profile across the rebar, on the onset of depassivation is shown in Fig. 6c2 where a sharp peak denotes the change of current from passive to active state.

At this location, the activated anodic and cathodic reactions lead to a quick consumption of the available oxygen, thus limiting the corrosion current. Once the immediately available oxygen is depleted, the corrosion process is set to be under concentration control. The magnitude of the post-peak corrosion density can be observed from Fig. 6c1 and is equal to 0.002 A/m².

Chloride ingress through the bulk leads to the attainment of the critical chloride threshold equal to $f^p_{Cl\_T} = 0.42$ (%W_{binder}), thereby creating another activation zone, after 22.5 years. The rebar corrosion current distribution is shown in Fig. 6d2. The time evolution of corrosion current at location 2 is shown in Fig. 6d1. An initial current of 2.15×10^{-4} A/m² is achieved which increases gradually, reaching a limiting current similar to that of the first activation spot, thereby sharing the incoming oxygen with the location 1. The effect of the increase in current at location 2 in Fig. 6d1 can be observed in the post peak current at location 1 in Fig. 6c1 after 22.5 years, where the effect of consumption of oxygen at an adjacent location is seen by a slight reduction of current. It is possible, that after a sufficiently long time and under an increasing chloride ingress, a sufficient amount of chloride is accumulated at all points on the rebar, so that the rebar would experience uniform corrosion.

Figure 7 shows the electrolyte current density along the rebar surface. At the end of the initiation stage (14.35 years) in Fig. 7a, a peak electrolyte current density is attained, which eventually reduces to a limiting current due to oxygen consumption. Correspondingly, a second peak is achieved, marking the passing of the second chloride threshold. Thus, the entire rebar dynamics have been defined as a combination of a random chloride threshold function $f^p_{Cl\_T}$. Such an approach leads to new
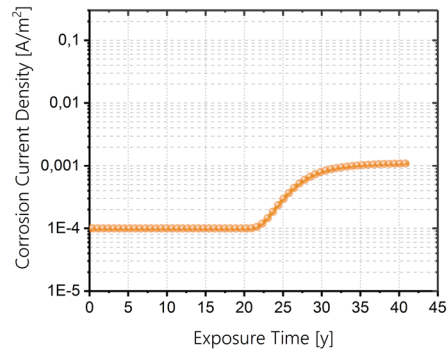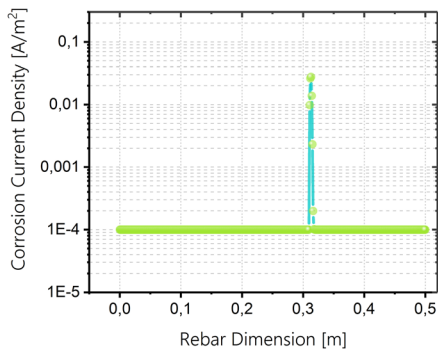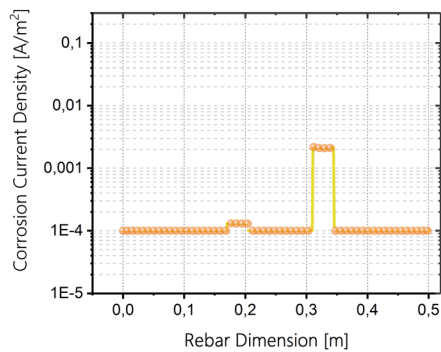
Mir *et al. Int J Concr Struct Mater*   (2019) 13:11

Page 12 of 18
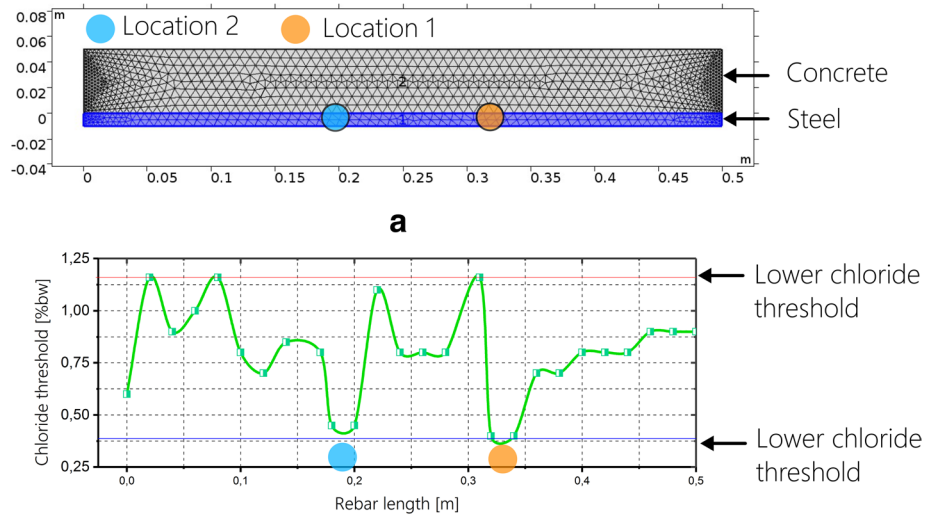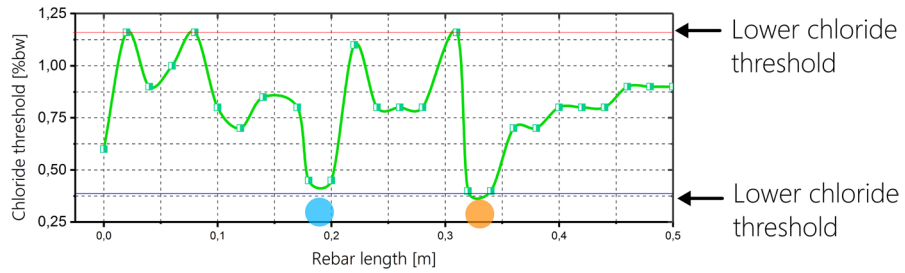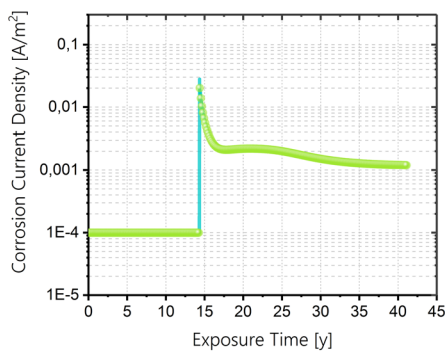
Fig. 6 **a** 2D numerical model with triangular elements. Current evolutions are monitored at locations 1 and 2. **b** Random varying chloride threshold applied at rebar surface. Alonso et al. (2000) with $0.39 < Cl_{th} < 1.16$ (free Cl^- as %binder weight). **c1** Evolution of current density at location 1 with time. **c2** Current density at location 1 on the onset of depassivation. **d1** Time evolution of current density at location 2. **d2** Corrosion current density at location 2 on the onset of depassivation at location 2.

Mir *et al. Int J Concr Struct Mater* (2019) 13:11

Page 13 of 18

Fig. 7 Evolution of electrolyte current density with exposure time: **a** 14.35 years, **b** 22.5 years, **c** 35 years and **d** 41 years. The cover used in this simulation is 50 mm.
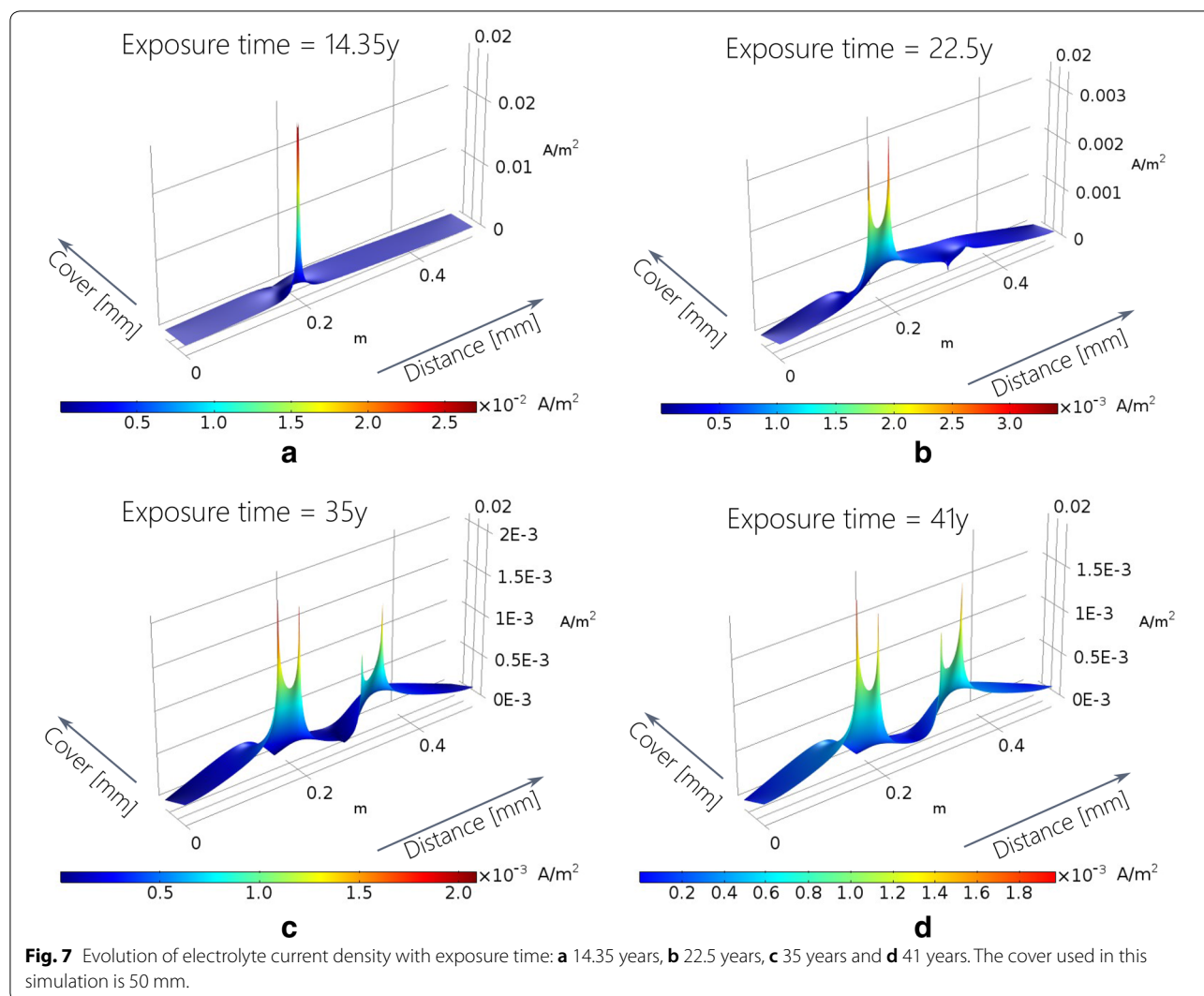
Table 3 Polarization data used in the model has been adopted from works of Kranc and Sagues (2001).

Parameter	Anodic	Cathodic	Unit
Exchange current density (i^0)	1.875×10^{-4}	6.25×10^{-6}	A/m^2
Tafel slope (β)	60	-160	V/dec
Equilibrium potential ($\emptyset^0$)	-780	160	mV/SCE

possibilities in research as $f^p_{Cl\_T}$ can act as central factor against which other randomly varying factors of Steel–Concrete Interface can be weighed against.

4.2 Effect of Chloride Transport and Cover on Initiation Time

The chloride diffusion values have been taken (Johannesson et al. 2007) and corrected for tortuosity (Table 3).

However, further corrections of the diffusion coefficients may be required to account for the dependence of diffusion coefficient on concentrations gradients (Snyder et al. 2003). Other effects include the influence of temperature on the activation energy of diffusion process, as reported by the experimental investigation of Lin (1993). The present model does not consider these effects. For the sake of simplicity, and to keep the discussion around variable threshold and the underlying computational architecture, only microstructure corrections (Johannesson et al. 2007) have been accounted in the model. Recent discussions about the pore system inside concrete and associated diffusion corrections have been provided by Yang et al. (2017).

Although, it has been previously discussed that the initiation time is dependent on local Steel–Concrete Interface conditions as reflected by $f^p_{Cl\_T}$, other factors could play a significant role. Deeply placed rebars usually suffer

Mir *et al. Int J Concr Struct Mater* (2019) 13:11

Page 14 of 18

less from chloride-induced corrosion. These rebars might still contribute cathodically in a macrocell configuration. Hence, cover distance as well as the quality of concrete are important factors. Parameter studies were carried out by varying diffusion coefficient of chloride against cover distance. A dense, tightly compacted concrete leads to a lower diffusion of chloride compared to a loosely packed concrete and the chosen values reflect it. It is also obvious that reducing the cover decreases the initiation time and a decrease in the chloride diffusion coefficient leads to an

elongation of the initiation time. Parameter studies were carried out with cover ranging from 25 to 75 mm and chloride diffusivity $(1.5–6) * 10^{-12}$ m^2/s and are presented in Fig. 8. Values with error bars represent simulations where the initiation time lasted more than final simulation time of 41 years. Apart from these, many other factors govern the length of the initiation stage and it is very difficult to study the effect of each one independently.

4.3 Chloride Profiles

Figure 9a, b show the evolution over time chloride profiles across penetration depth in saturated concrete. Chlorides bind to CSH structures along the influx path. The bound chlorides increases gradually with time with a similar profile as compared to free chloride concentration in solution. The characteristic chloride peak (Ozbolt et al. 2016) does not show up due to a saturated influx of macro-capillary water in submerged zone: no wetting and drying of the exposure face is considered. Furthermore, sudden crack opening events can also lead to sharp peaks in the profile.

4.4 Model Comparison

Figure 10a refers to the average corrosion current density at the anode across various degrees of saturation. The computational results are compared with the experimental works of Lopez and Gonzalez (1993) and Michel (2013) and a good agreement is observed. For the case presented in this paper, i.e. submerged zone exposure (saturated conditions), lower corrosion currents (0.015 A/m^2 for saturated case) are reported as compared to critical saturation range of 75–85%. Furthermore

Fig. 8 A qualitative variation of initiation time with concrete quality and placement of rebar from the exposure surface.
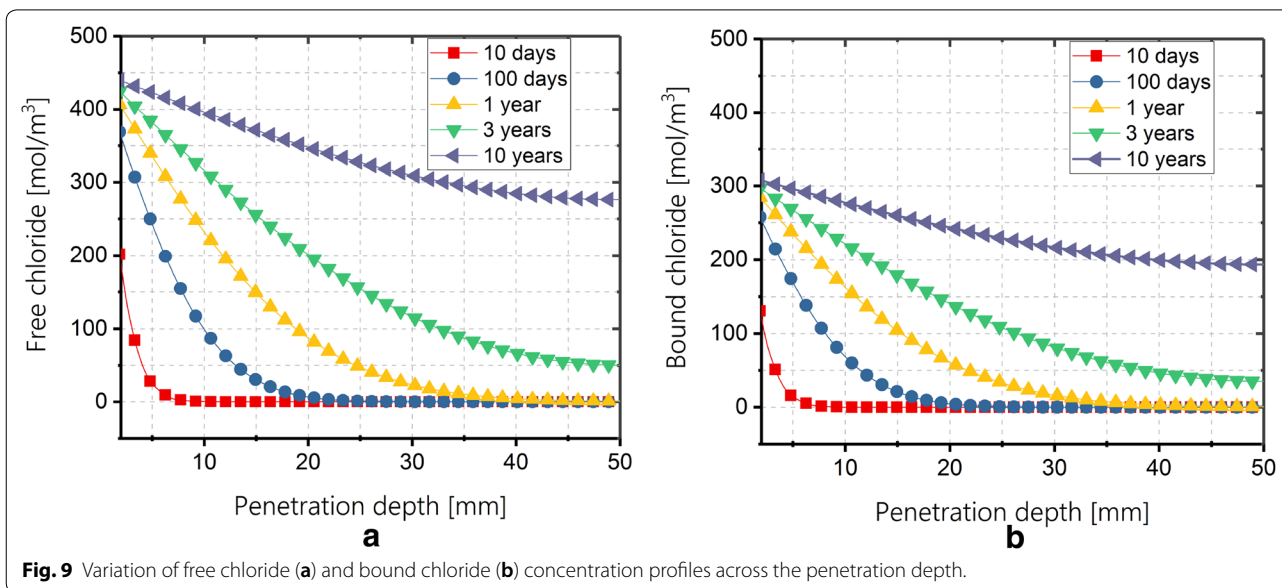
Fig. 9 Variation of free chloride (**a**) and bound chloride (**b**) concentration profiles across the penetration depth.

Mir *et al. Int J Concr Struct Mater*   (2019) 13:11

Page 15 of 18

Fig. 10 a Comparison of average corrosion current density at the activated area and comparison with works of Michel (2013) and Lopez and Gonzalez (1993) across different ranges of saturation. **b** Parametric studies of corrosion current for w/c 0.4 and 0.7 across different ranges of saturation.
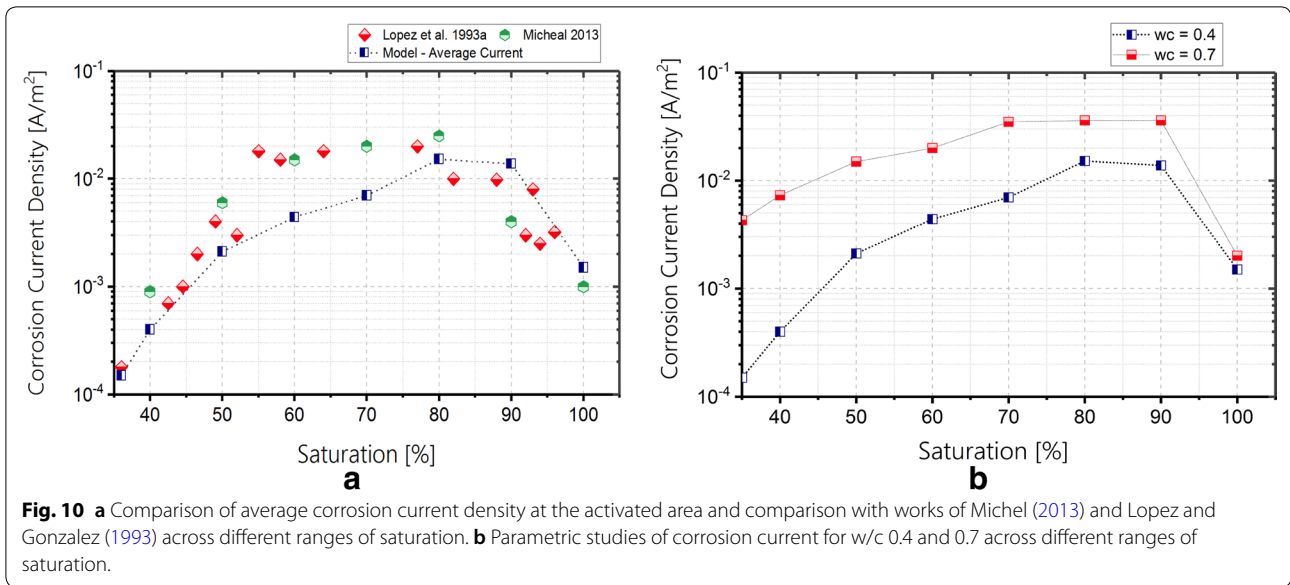
saturated values less than 50% also depict a lower corrosion current due to increasing resistivity of concrete. Another important parameter governing the corrosion rate in reinforced concrete is the water-to-binder (w/c) ratio. Parameter studies are presented for w/c ratio of 0.4 and 0.7 across various degrees of saturation. Higher corrosion currents are observed for higher w/c ratio as shown in Fig. 10b.

5 Conclusion

1. The study presents a continuum based corrosion model, which is a coupled model in terms of transport of species, moisture, heat transport and coupled electrochemistry. The model is able to simulate processes before and after corrosion initiation. The broader aim of this study is to predict the service life of infrastructure in the submerged marine zone.
2. The model is able to simulate the transition between passivated to depassivated stage based on localized chloride threshold values. Development and subsequent evolution of anodic regions on the rebar is presented likewise.
3. Equations have been presented for governing non-mechanical processes leading to rebar corrosion. This includes capillary water transport, chloride transport and its binding with the matrix, transport of oxygen and other pore solution species, and as well as coupled electrochemistry. These equations are solved with finite element method.
4. A major objective of this study is to develop models to predict the behavior of new concrete recipe for

marine infrastructure. Simulations show that oxygen is able to sustain localized active areas on the rebar surface. However, the current density is dependent on the availability of oxygen and thus limited to around 0.0015 A/m^2 in the saturated cases. Comparison with previous models and experiments are reported. The macrocell coupling of the region of interest to other oxygen rich areas i.e. splash zone is not a part of the study and will be dealt in future.

6 Future Scope

a. It is possible that with an evolution of conditions at the SCI, such as chloride content, oxygen content, pH, and temperature across the service life of the structure lead to a change in the electrochemical parameters, i.e. time evolution of corrosion parameters. In our ongoing experiments, it was observed that electrochemical parameters change dynamically inside concrete as it ages. These supporting experimental results will be reported in the future versions of the this model.
b. The localization of corrosion onset is modelled by a random theoretical function. However random varying threshold function is based solely on a threshold range. However, other empirical and statistical relations might be developed which could describe more explicitly randomly occurring phenomena at the rebar interface.
c. Due to the long experimentation times, chloride diffusion parameters were taken from relevant litera-

Mir *et al. Int J Concr Struct Mater*   (2019) 13:11

Page 16 of 18

ture. An exact quantitative benefit from the current model can only be derived for our particular concrete recipe by using actual data from experimentation. However, completion of migration tests to derive effective chloride diffusivity are in progress and will be reported in future experimental studies. Correspondingly, the model will also be updated.

d. Effect of presence of pre-cracks and crack generation due to oxide growth have not been included in the model, and will be studied in future.

Abbreviations
SCI: Steel–Concrete Interface; RC: reinforced concrete; FEM: finite element method; CSH: calcium silicate hydrate; AFm: alumina ferric oxide mono-sulfate.

Authors' contributions
ZMM, DH, CG, RS, ACB, PM devised the main conceptual idea, discussed the numerical strategy, evaluated the results and contributed in drafting the script. MGSF and MLZ supervised the work and gave critical comments to this manuscript. All authors discussed and contributed to the final manuscript. All authors read and approved the final manuscript.

Author details
[1] Institute of Materials Research, Helmholtz-Zentrum Geesthacht Centre for Materials and Coastal Research, Max-Planck Str. 1, 21502 Geesthacht, Schleswig-Holstein, Germany. [2] Faculty of Mechanical Engineering, Helmut-Schmidt University, 22008 Hamburg, Germany. [3] Department of Materials and Ceramic Engineering and CICECO, University of Aveiro, 3810-193 Aveiro, Portugal. [4] SINTEF Materials and Chemistry, 7465 Trondheim, Norway. [5] Faculty of Engineering, University of Kiel, Kaiserstrasse 2, 24143 Kiel, Germany.

Competing interests
The authors declare that they have no competing interests.

Availability of data and materials
The numerical model developed in this study will be shared on request and after the approval of all authors is obtained.

References
Alonso, C., Andrade, C., Castellote, M., & Castro, P. (2000). Chloride threshold values to depassivate reinforcing bars embedded in a standardized OPC mortar. *Cement and Concrete Research, 30*(7), 1047–1055.

Andrade, C., Diez, L. M., & Alonso, C. (1997). Mathematical modeling of a concrete surface "skin effect" on diffusion in chloride contaminated media. *Advanced Cement Based Materials, 6*(2), 39–44.

Angst, U. (2018). Challenges and opportunities in corrosion of steel in concrete. *Materials and Structures, 51*, 4.

Angst, U., & Elsener, B. (2015). Forecasting chloride-induced reinforcement corrosion of concrete-effect of realistic reinforcement steel surface conditions. In *4th international conference on concrete, repair, rehabilitation and retrofitting (ICCCRRR), Leipzig, Germany*.

Angst, U. M., & Elsener, B. (2017). The size effect in corrosion greatly influences the predicted life span of concrete infrastructures. *Science Advances, 3*(8), e1700751.

Angst, U., Elsener, B., Larsen, C. K., & Vennesland, O. (2009). Critical chloride content in reinforced concrete—A review. *Cement and Concrete Research, 39*(12), 1122–1138.

Angst, U. M., Geiker, M. R., Michel, A., Gehlen, C., Wong, H., Isgor, O. B., et al. (2017). The steel–concrete interface. *Materials and Structures, 50*(2), 143.

Balabanic, G., Bicanic, N., & Durekovic, A. (1996). The influence of w/c ratio, concrete cover thickness and degree of water saturation on the corrosion rate of reinforcing steel in concrete. *Cement and Concrete Research, 26*(5), 761–769.

Bazant, Z. P. (1979). Physical model for steel corrosion in concrete sea structures—Theory. *Journal of the Structural Division-ASCE, 105*(6), 1137–1153.

Belytschko, T., Liu, W. K., & Moran, B. (2000). *Nonlinear finite elements for continua and structures*. New York: Wiley.

Belytschko, T., Liu, W. K., Moran, B., & Elkhodary, K. I. (2014). *Nonlinear finite elements for continua and structures* (2nd ed.). Chichester: Wiley.

Bertolini, L., Elsener, B., Pedeferri, P., Redaelli, E., & Polder, R. B. (2013). *Corrosion of steel in concrete: Prevention, diagnosis, repair*. New York: Wiley-VCH.

Bischoff, M., Ramm, E., & von Scheven, M. (2014). *Advanced computational structural mechanics—Lecture Notes*. Stuttgart: Institut für Baustatik und Baudynamik, University of Stuttgart.

Borosnyói, A., & Balázs, G. L. (2005). Models for flexural cracking in concrete: The state of the art. *Structural Concrete, 6*(2), 53–62.

Boubitsas, D., Luping, T., & von Utgenannt, P. (2014). *Chloride ingress in concrete exposed to marine environment—Field data up to 20 years' exposure*. Stockholm: Swedish Cement and Concrete Research Institute (CBI).

British Cement Association. (1997). *Development of a holistic approach to ensure the durability of new concrete construction*.

Cadoni, E., Dotta, M., Forni, D., Tesio, N., & Albertini, C. (2013). Mechanical behaviour of quenched and self-tempered reinforcing steel in tension under high strain rate. *Materials and Design, 49*, 657–666.

Castel, A., Vidal, T., Francois, R., & Arliguie, G. (2003). Influence of steel–concrete interface quality on reinforcement corrosion induced by chlorides. *Magazine of Concrete Research, 55*(2), 151–159.

Castel, A., Vidal, T., Viriyametanont, K., & Francois, R. (2006). Effect of reinforcing bar orientation and location on bond with self-consolidating concrete. *ACI Structural Journal, 103*(4), 559–567.

Deslouis, C., Festy, D., Gil, O., Maillot, V., Touzain, S., & Tribollet, B. (2000). Characterization of calcareous deposits in artificial sea water by impedances techniques: 2-deposit of Mg(OH)(2) without CaCO3. *Electrochimica Acta, 45*(11), 1837–1845.

Feng, X. G., Tang, Y. M., & Zuo, Y. (2011a). Influence of stress on passive behaviour of steel bars in concrete pore solution. *Corrosion Science, 53*(4), 1304–1311.

Mir *et al. Int J Concr Struct Mater* (2019) 13:11

Page 17 of 18

Feng, X. G., Zuo, Y., Tang, Y. M., Zhao, X. H., & Lu, X. Y. (2011b). The degradation of passive film on carbon steel in concrete pore solution under compressive and tensile stresses. *Electrochimica Acta, 58,* 258–263.

Ghods, P., Isgor, O. B., McRae, G. A., Li, J., & Gu, G. P. (2011). Microscopic investigation of mill scale and its proposed effect on the variability of chloride-induced depassivation of carbon steel rebar. *Corrosion Science, 53*(3), 946–954.

Ghods, P., Isgor, O. B., Mcrae, G., & Miller, T. (2009). The effect of concrete pore solution composition on the quality of passive oxide films on black steel reinforcement. *Cement & Concrete Composites, 31*(1), 2–11.

Gjorv, O. E. (1995). Effect of condensed silica fume on steel corrosion in concrete. *ACI Materials Journal, 92*(6), 591–598.

Glass, G. K., & Buenfeld, N. R. (2000). The influence of chloride binding on the chloride induced corrosion risk in reinforced concrete. *Corrosion Science, 42*(2), 329–344.

Hansson, C. M. (1984). Comments on electrochemical measurements of the rate of corrosion of steel in concrete. *Cement and Concrete Research, 14*(4), 574–584.

Hansson, C. M., Poursaee, A., & Laurent, A. (2006). Macrocell and microcell corrosion of steel in ordinary Portland cement and high performance concretes. *Cement and Concrete Research, 36*(11), 2098–2102.

Hirao, H., Yamada, K., Takahashi, H., & Zibara, H. (2005). Chloride binding of cement hydrates by binding isotherms of hydrates. *Journal of Advanced Concrete Technology, 3*(1), 77–84.

Höche, D. (2015). Simulation of corrosion product deposit layer growth on bare magnesium galvanically coupled to aluminum. *Journal of the Electrochemical Society, 162*(1), C1–C11.

Horne, A. T., Richardson, I. G., & Brydson, R. M. D. (2007). Quantitative analysis of the microstructure of interfaces in steel reinforced concrete. *Cement and Concrete Research, 37*(12), 1613–1623.

Ishida, T., Iqbal, P. O., & Anh, H. T. L. (2009). Modeling of chloride diffusivity coupled with non-linear binding capacity in sound and cracked concrete. *Cement and Concrete Research, 39*(10), 913–923.

Jakobsen, U. H., De Weerdt, K., & Geiker, M. R. (2016). Elemental zonation in marine concrete. *Cement and Concrete Research, 85,* 12–27.

Johannesson, B., Yamada, K., Nilsson, L. O., & Hosokawa, Y. (2007). Multi-species ionic diffusion in concrete with account to interaction between ions in the pore solution and the cement hydrates. *Materials and Structures, 40*(7), 651–665.

Karadakis, K., Azad, V. J., Ghods, P., & Isgor, O. B. (2016). Numerical investigation of the role of mill scale crevices on the corrosion initiation of carbon steel reinforcement in concrete. *Journal of the Electrochemical Society, 163*(6), C306–C315.

Kim, C. Y., & Kim, J. K. (2008). Numerical analysis of localized steel corrosion in concrete. *Construction and Building Materials, 22*(6), 1129–1136.

Koch, G. H., Brongers, M. P. H., Thompson, N. G., Virmani, Y. P., & Payer, J. H. (2001) *Corrosion costs and preventive strategies in the United States. FHWA-RD-01-156.*

Kranc, S. C., & Sagues, A. A. (1994). Computation of reinforcing steel corrosion distribution in concrete marine bridge substructures. *Corrosion, 50*(1), 50–61.

Kranc, S. C., & Sagues, A. A. (2001). Detailed modeling of corrosion macrocells on steel reinforcing in concrete. *Corrosion Science, 43*(7), 1355–1372.

Leech, C., Lockington, D., & Dux, P. (2003). Unsaturated diffusivity functions for concrete derived from NMR images. *Materials and Structures, 36*(260), 413–418.

Lin, S. H. (1993). Chloride diffusion in porous concrete under conditions of variable-temperature. *Warme Und Stoffubertragung-Thermo and Fluid Dynamics, 28*(7), 411–415.

Lindvall, A. (2003). *Environmental actions on concrete exposed in marine and road environments and its response*. Ph.D. thesis, Chalmers University of Technology.

Lopez, W., & Gonzalez, J. A. (1993). Influence of the degree of pore saturation on the resistivity of concrete and the corrosion rate of steel reinforcement. *Cement and Concrete Research, 23*(2), 368–376.

Marsavina, L., Audenaert, K., Schutter, G., Faur, N., & Marsavina, D. (2009). Experimental and numerical determination of the chloride penetration in cracked concrete. *Construction and Building Materials, 23*(1), 264–274.

Martin-Perez, B. (1999). Service life modelling of R.C. highway structures exposed to chlorides, PhD Thesis. University of Toronto, National Library of Canada = Bibliothèque nationale du Canada. http://www.collection scanada.ca/obj/s4/f2/dsk1/tape8/PQDD_0007/NQ41230.pdf. http://hdl.handle.net/1807/13268.

Michel, A. (2013). *Reinforcement corrosion: numerical simulation and service life prediction*. Ph.D. thesis, Technical University of Denmark (DTU).

Mohammed, T. U., Otsuki, N., Hamada, H., & Yamaji, T. (2002). Chloride-induced corrosion of steel bars in concrete with presence of gap at steel–concrete interface. *ACI Materials Journal, 99*(2), 149–156.

Nikolaou, J., & Papadimitriou, G. D. (2004). Microstructures and mechanical properties after heating of reinforcing 500 MPa class weldable steels produced by various processes (Tempcore, microalloyed with vanadium and work-hardened). *Construction and Building Materials, 18*(4), 243–254.

Oluwadare, G. O., & Agbaje, O. (2007). Corrosion of steels in steel reinforced concrete in cassava juice. *Journal of Applied Sciences, 7,* 2474–2479.

Ozbolt, J., Balabanic, G., & Kuster, M. (2011). 3D numerical modelling of steel corrosion in concrete structures. *Corrosion Science, 53*(12), 4166–4177.

Ozbolt, J., Balabanic, G., Periskic, G., & Kuster, M. (2010). Modelling the effect of damage on transport processes in concrete. *Construction and Building Materials, 24*(9), 1638–1648.

Ozbolt, J., Orsanic, F., & Balabanic, G. (2014). Modeling pull-out resistance of corroded reinforcement in concrete: Coupled three-dimensional finite element model. *Cement & Concrete Composites, 46,* 41–55.

Ozbolt, J., Orsanic, F., & Balabanic, G. (2016). Modeling influence of hysteretic moisture behavior on distribution of chlorides in concrete. *Cement & Concrete Composites, 67,* 73–84.

Ozbolt, J., Orsanic, F., Balabanic, G., & Kuster, M. (2012). Modeling damage in concrete caused by corrosion of reinforcement: Coupled 3D FE model. *International Journal of Fracture, 178*(1–2), 233–244.

Page, C. L. (1975). Mechanism of corrosion protection in reinforced-concrete marine structures. *Nature, 258*(5535), 514–515.

Page, C. L., Short, N. R., & Eltarras, A. (1981). Diffusion of chloride-ions in hardened cement pastes. *Cement and Concrete Research, 11*(3), 395–406.

Poursaee, A. (2016). Temperature dependence of the formation of the passivation layer on carbon steel in high alkaline environment of concrete pore solution. *Electrochemistry Communications, 73,* 24–28.

Poursaee, A., & Hansson, C. M. (2007). Reinforcing steel passivation in mortar and pore solution. *Cement and Concrete Research, 37*(7), 1127–1133.

Ray, A., Mukherjee, D., Sen, S. K., Bhattacharya, A., Dhua, S. K., Prasad, M. S., et al. (1997). Microstructure and properties of thermomechanically strengthened reinforcement bars: A comparative assessment of plain-carbon and low-alloy steel grades. *Journal of Materials Engineering and Performance, 6*(3), 335–343.

Saetta, A. V., Scotta, R. V., & Vitaliani, R. V. (1993). Analysis of chloride diffusion into partially saturated concrete. *ACI Materials Journal, 90*(5), 441–451.

Sagüés, A. A., Sanchez, A. N., Lau, K., & Kranc, S. C. (2014). Service life forecasting for reinforced concrete incorporating potential-dependent chloride threshold. *Corrosion, 70*(9), 942–957.

Scully, J. R., & Hurley, M. F. (2007). *Investigation of the corrosion propogation characteristics of new metallic reinforcing bars—Final Contract Report VTRC 07-CR9.*

Silva, N., Tang, L., Lindqvist, J. E., & Boubitsas, D. (2013). Chloride profiles along the concrete–steel interface. *International Journal of Structural Engineering, 4*(1–2), 100–112.

Snyder, K. A., Feng, X. G., Keen, B. D., & Mason, T. O. (2003). Estimating the electrical conductivity of cement paste pore solutions from OH^-, K^+, Na^+ concentrations. *Cement and Concrete Research, 33,* 793–798.

Soylev, T. A., & Francois, R. (2003). Quality of steel–concrete interface and corrosion of reinforcing steel. *Cement and Concrete Research, 33*(9), 1407–1415.

Stefanoni, M., Angst, U., & Elsener, B. (2015). Local electrochemistry of reinforcement steel—Distribution of open circuit and pitting potentials on steels with different surface condition. *Corrosion Science, 98,* 610–618.

Tang, L., & Nilsson, L.-O. (1996). Service life prediction of concrete structures under seawater by a numerical approach. *Durability of Building Materials and Components, 7*(1), 97–106.

Thomas, M. D. A., & Bamforth, P. B. (1999). Modelling chloride diffusion in concrete—Effect of fly ash and slag. *Cement and Concrete Research, 29*(4), 487–495.

Tuutti, K. (1982). *Corrosoion of steel in concrete. Technical Report.* Stockholm: Swedish Cement and Concrete Research Institute.

Vera, R., Villarroel, M., Carvajal, A. M., Vera, E., & Ortiz, C. (2009). Corrosion products of reinforcement in concrete in marine and industrial environments. *Materials Chemistry and Physics, 114*(1), 467–474.

Mir *et al. Int J Concr Struct Mater*   (2019) 13:11

Page 18 of 18

Vollpracht, A., Lothenbach, B., Snellings, R., & Haufe, J. (2016). The pore solution of blended cements: A review. *Materials and Structures, 49*(8), 3341–3367.

Walsh, M. T. (2015). *Corrosion of steel in submerged concrete structures*. Ph.D. thesis, University of South Florida. Retrieved from http://scholarcommons.usf.edu/etd/6048.

Yamashita, M., Konishi, H., Kozakura, T., Mizuki, J., & Uchida, H. (2005). In situ observation of initial rust formation process on carbon steel under Na_2SO_4 and NaCl solution films with wet/dry cycles using synchrotron radiation X-rays. *Corrosion Science, 47*(10), 2492–2498.

Yan, J. F., Nguyen, T. V., White, R. E., & Griffin, R. B. (1993). Mathematical-modeling of the formation of calcareous deposits on cathodically protected steel in seawater. *Journal of the Electrochemical Society, 140*(3), 733–742.

Yang, P., Sant, G., & Neithalath, N. (2017). A refined, self-consistent Poisson–Nernst–Planck (PNP) model for electrically induced transport of multiple ionic species through concrete. *Cement & Concrete Composites, 82,* 80–94.

Zhang, T. W., & Gjorv, O. E. (1996). Diffusion behavior of chloride ions in concrete. *Cement and Concrete Research, 26*(6), 907–917.

Zhang, Y., & Poursaee, A. (2015). Passivation and corrosion behavior of carbon steel in simulated concrete pore solution under tensile and compressive stresses. *Journal of Materials in Civil Engineering, 27*(8), 04014234.

Zibara, H. (2001). *Binding of external chlorides by cement pastes*. Ph.D. thesis, University of Toronto.

Zienkiewicz, O. C. (1972). 'Finite elements of non-linear continua, J. T. Oden, McGraw-Hill, New York, 1972. Price $8.40. *International Journal for Numerical Methods in Engineering, 5*(1), 148. https://doi.org/10.1002/nme.1620050117/abstract.